EES Catalysis

Accepted Manuscript

This article can be cited before page numbers have been issued, to do this please use: J. Jeon, S. Kim, M. G. Ha, D. Kim , H. Bang, Y. Ko, J. Choi, D. Whang, W. H. Lee and H. Oh, *EES Catal.*, 2026, DOI: 10.1039/D6EY00070C.

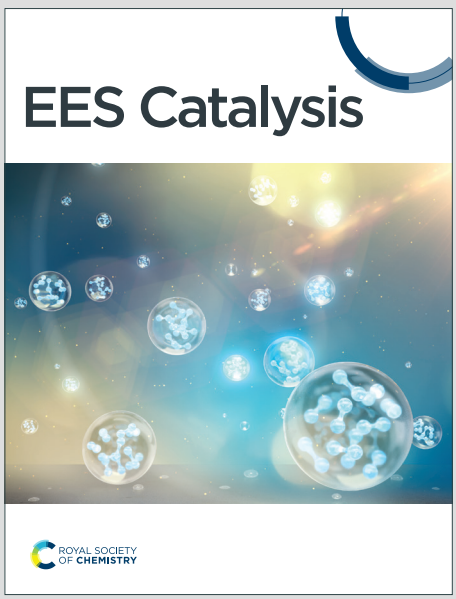

View Article Online
DOI: 10.1039/D6EY00070C

Broader context statement

The electrochemical CO_2 reduction reaction (CO_2RR) is a cornerstone technology for achieving global carbon neutrality by converting waste emissions into high-value chemical feedstocks such as ethylene. However, the transition from laboratory-scale experiments to industrial-scale deployment is currently limited by the instability of active catalytic sites and low selectivity at high current densities. This work addresses these challenges through a "precursor engineering" strategy, demonstrating that the identity of the precursor anion (chloride vs. sulfate) is a decisive factor in determining the catalyst's final performance. By incorporating chloride ions as functional dopants, we successfully stabilized active Cu^+ sites and induced the formation of defect-rich structures that favor C–C coupling. Our catalyst achieved a 31% ethylene Faradaic efficiency in a large-area (25 cm^2) electrolyzer at high current densities, marking a significant step toward practical CO_2 valorization. These findings highlight the overlooked potential of precursor-derived dopants as a simple yet effective tool for modulating catalyst electronic structures, providing a clear pathway for the mass production of robust electrocatalysts for a cleaner and more sustainable chemical industry.

View Article Online
DOI: 10.1039/D6EY00070C

ARTICLE

Scalable Synthesis of Chloride-Mediated Copper Nanocatalysts for Selective Ethylene Production in Large-Area CO_2 Electrolyzers

Received 00th January 20xx,
Accepted 00th January 20xx

DOI: 10.1039/x0xx00000x

Jiho Jeon,[†a] Sohui Kim,[†a,b] Min Gwan Ha,[c] Dogyeong Kim,[a] Hyeon-Seok Bang,[a,b] Young-Jin Ko,[d] Jae-Young Choi,[b] Dongmok Whang,*[b] Woong-Hee Lee,*[a] Hyung-Suk Oh,*[a,b,e]

Copper-based electrocatalysts are essential for the electrochemical reduction of CO_2 to ethylene; however, preventing the rapid reduction of active Cu^+ species and suppressing the competing hydrogen evolution reaction remain key challenges. Herein, we demonstrate that precursor engineering is a decisive strategy for modulating the electronic structure and catalytic selectivity of Cu nanoparticles (NPs). Using a scalable wet-chemical reduction method, we synthesized chloride-incorporated Cu NPs (Cu-Cl NPs) on a gram scale. In a large-area (25 cm^2) membrane electrode assembly electrolyzer, the Cu-Cl NPs achieved a peak ethylene Faradaic efficiency of 31% at 400 mA cm^{-2}, markedly outperforming sulfate-derived counterparts. *Operando* X-ray absorption fine structure analysis and *in situ* Raman spectroscopy revealed that chloride dictates the unique surface reconstruction, maintaining the Cu^0/Cu^{1+} interface even at high current densities. These persistent Cl-stabilized Cu^+ sites improved catalytic performance. This structural evolution steers the reaction pathway toward selective C_2H_4 formation by promoting C–C coupling over competing hydrogen evolution reaction, highlighting the overlooked potential of precursor anions as functional dopants and offering a facile route to design robust electrocatalysts for industrial-scale CO_2 valorization.

Introduction

The electrochemical carbon dioxide reduction reaction (CO_2RR) has emerged as a pivotal technology for addressing the global climate crisis by achieving carbon neutrality while converting the captured CO_2 into high-value-added chemicals[1-11]. Among the various reduction products, ethylene (C_2H_4), a multicarbon (C^{2+}) product, serves as a fundamental feedstock for synthesizing polymers such as polyethylene and holds considerable economic importance in the chemical industry[12-16]. However, conventional fossil-fuel-based steam cracking processes suffer from critical drawbacks, including substantial energy consumption owing to high operating temperatures and substantial greenhouse gas emissions[17, 18]. By contrast, electrochemical C_2H_4 production has gained prominence as compelling sustainable alternative, as the process operates on electricity, enabling seamless integration with renewable energy sources such as solar and wind power[19-21].

To date, Cu remains the only monometallic catalyst capable of facilitating C–C coupling of CO intermediates to produce C_2H_4[12, 13, 22-25]. However, Cu catalysts face considerable challenges in practical applications, primarily because of their broad product distribution encompassing byproducts such as CO and H_2, resulting in low C_2H_4 selectivity. Furthermore, the current catalysts often fail to simultaneously achieve the high current density and low overpotential required for industrial implementation. To address these limitations, extensive research has focused on optimizing the active sites through surface structure control, facet engineering, and defect manipulation[26-32]. Particularly, the coexistence of surface Cu^+ and Cu^0 oxidation states has been identified as a key factor in lowering the activation energy of CO dimerization and promoting C–C coupling[23, 33-37]. Nevertheless, because thermodynamically unstable Cu^+ species are prone to reduction to metallic Cu^0 under strong reducing potentials, maintaining the stability of Cu^+ species during the reaction remains a critical challenge in the development of high-performance catalysts[38-40].

Previous studies have attempted to stabilize these active sites by employing strategies, such as alloying[41-43], support modification[44-46], or oxide-derived Cu structures[47, 48]. In addition to these conventional approaches, the selection of precursor salts offers a promising, yet underexplored avenue for modulating the electronic states of the catalyst. Specifically, the anions inherent in the precursors can serve as effective dopants that directly influence the oxidation state of the metal. However, this aspect has been largely overlooked, as most studies have concentrated on the physical properties of the final catalyst, such as particle size. The nonmetallic components of the precursor are generally assumed to be impurities that are completely removed during synthesis. Contrarily, we

[a] Clean Energy Research Center,Korea Institute of Science and Technology, Seoul, Republic of Korea. E-mail: hyung-suk.oh@kist.re.kr, abcabac@kist.re.kr
[b] Dept. of Advanced Materials Science and Engineering, Sungkyunkwan University, Suwon, Republic of Korea. E-mail: dwhang@skku.edu
[c] Hydrogen Demonstration Research Center, Korea Institute of Energy Research, Buan, Republic of Korea.
[d] Yonsei University, Division of Environmental and Energy Engineering
[e] KIST-SKKU Carbon-Neutral Research Center, Sungkyunkwan University (SKKU), Republic of Korea
† These authors contribute equally as first authors.

View Article Online
DOI: 10.1039/D5EY00070C

demonstrated that halide ions from precursors such as $CuCl_2$ can be retained as substitutional dopants even after thorough washing. These incorporated ions play a pivotal role in modifying the electronic structure of the Cu surface and maintaining Cu^+ in its otherwise thermodynamically unstable oxidation state. This electronic modification is critical for enhancing CO adsorption and suppressing the competing hydrogen evolution reaction, thereby markedly improving C_2H_4 selectivity.

In this study, we synthesized chloride-incorporated Cu nanoparticles (NPs) using a $CuCl_2$ precursor and evaluated their CO_2R performance in a large-area (10 cm^2) membrane electrode assembly (MEA) system. The results demonstrated a high C_2H_4 Faradaic efficiency (FE) of 28.2%, at an operating current of 5 A, confirming its potential for practical applications. Furthermore, through energy-dispersive X-ray spectroscopy (EDS), X-ray photoelectron spectroscopy (XPS), and *operando* X-ray absorption fine structure (XAFS) analysis—which enables real-time monitoring of the catalyst state under operating conditions—we elucidated the mechanism by which precursor-derived chloride ions stabilize Cu^+ species during the reaction and contribute to enhanced C_2H_4 selectivity.

Results and discussion

Cu NPs were synthesized via a facile wet-chemical reduction method using $NaBH_4$ as the reducing agent under ambient temperature and pressure conditions, as illustrated in **Fig. S1a**[49]. This approach is highly energy-efficient, as it eliminates the need for the high-temperature thermal treatment characteristics of conventional hydrothermal or pyrolysis processes. Furthermore, the surfactant-free synthesis simplifies the washing and purification steps, offering distinct advantages for scalable mass production. As a demonstration of scalability, the reaction proceeded in the liquid phase under ambient conditions, enabling the synthesis of approximately 1.1 g of NPs in a single laboratory-scale batch (**Fig. S1b**). To investigate the influence of precursor type, syntheses were conducted under otherwise identical conditions using $CuCl_2$ and $CuSO_4$ salts. Hereafter, the NPs synthesized from $CuCl_2$ and $CuSO_4$ are denoted as Cu-Cl NPs and Cu-SO_4 NPs, respectively. The synthesized particles were subjected to multiple centrifugation and washing cycles with deionized water and isopropyl alcohol to remove residual impurities, followed by freeze drying to minimize particle aggregation during the drying step. The dried NPs were then dispersed in isopropyl alcohol to form a catalyst ink, which was spray coated onto a carbon paper substrate to fabricate the working electrodes.

The morphology and microstructure of the synthesized NPs were characterized by scanning electron microscopy (SEM) and transmission electron microscopy (TEM). The SEM images revealed a distinct difference in particle size depending on the precursor (**Fig. S2**). Cu-Cl NPs consisted of particles ranging from 50 to 100 nm, whereas Cu-SO_4 NPs were considerably smaller, with an average diameter of approximately 20 nm. Consistent with the SEM observations, the low-magnification TEM images show that the Cu-Cl NPs exhibited a cubic-like morphology with an average size of 75 nm (**Fig. 1a–c, S3**). This morphology is consistent with previous reports, indicating that halide ions such as chloride promote preferential growth of the (100) facet. At higher magnification, a distinct passivation layer was observed on the particle surface. High-resolution TEM analysis

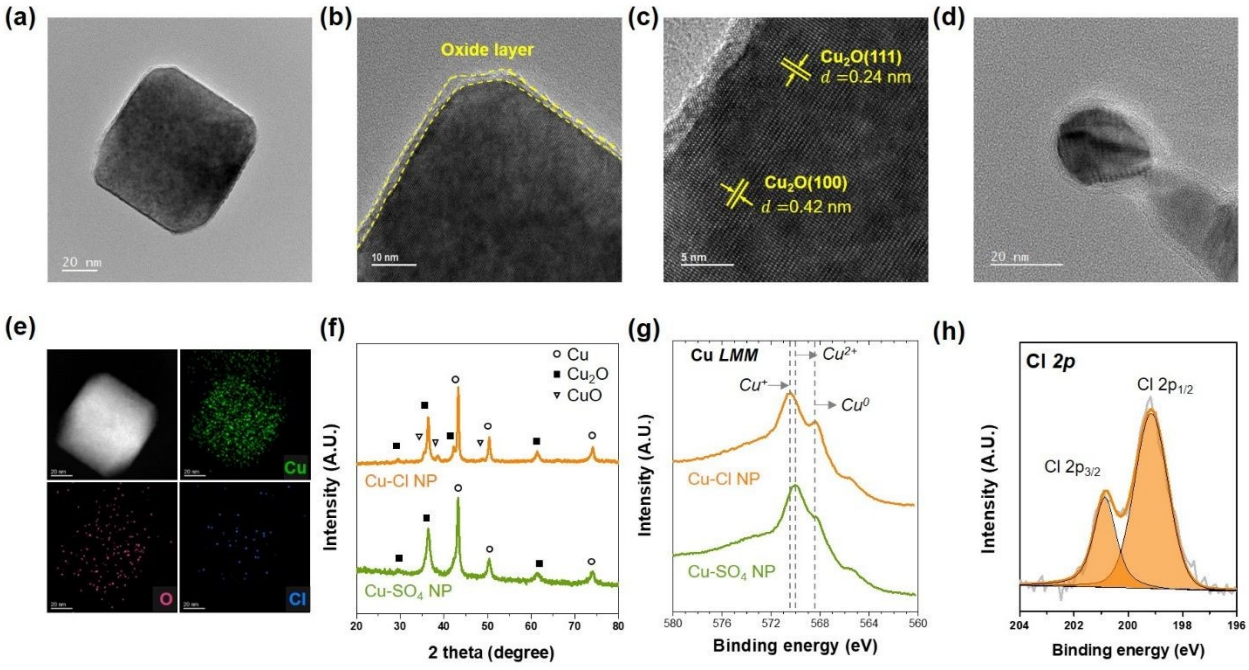

Fig. 1 Structural and surface characterizations of Cu-X NP electrodes. a, b) High-resolution TEM images of Cu-Cl NPs, c) interplanar d-spacing of Cu-Cl NP calculated from HR-TEM images, d) high-resolution TEM images of Cu-SO_4 NPs, e) STEM-EDS elemental mapping images of Cu-Cl NPs, f) XRD patterns of Cu-Cl and Cu-SO_4 NPs, g) XPS Cu 2p spectra of Cu-Cl and Cu-SO_4 NP, and h) XPS Cl 2p spectrum of Cu-Cl NPs

revealed clear lattice fringes with a d-spacing corresponding to the Cu_2O phase, indicating that the Cu-Cl NPs were synthesized with a surface structure closely resembling that of copper oxide. By contrast, the Cu-SO_4 NPs exhibited phase characteristics of typical metallic copper and an irregular quasi-spherical morphology (**Fig. 1d**). To further assess the effect of anion identity, Cu-Cl-SO_4 NPs were synthesized using a 1:1 mixture of $CuCl_2$ and $CuSO_4$. These particles displayed a hybrid morphology combining the highly crystalline uniformly sized character of Cu-Cl NPs with the irregular, spherical character of Cu-SO_4 NPs. Notably, Moiré patterns arising from the overlap of low-crystallinity grains were observed in these particles (**Fig. S5**).

To elucidate the compositional origins of these structural differences, TEM-EDS elemental mapping and quantitative analysis were performed (**Fig. 1e** and **S6–S10**). Elemental mapping confirmed a uniform distribution of Cl throughout the Cu-Cl NPs, whereas no S signal was detected in the Cu-SO_4 NPs. Notably, a discernible Cl signal was also observed for the Cu-Cl-SO_4 NPs alongside the S signal. Quantitative analysis further confirmed that a non-negligible amount of residual chloride (approximately 2 wt%) was present in the Cu-Cl NPs, with a trace amount retained in the Cu-Cl-SO_4 samples. Given that loosely physisorbed ions were effectively removed during the washing procedure, this finding implies that Cl is intrinsically retained within the Cu NPs and suggests that precursor-derived Cl anions play a critical role in structure formation, even in the presence of competing anions. Building on these compositional findings, X-ray diffraction (XRD) and XPS were performed to characterize the crystal structure and surface chemical states. XRD analysis revealed a mixed-phase composition characterized by the coexistence of metallic Cu, CuO, and Cu_2O (**Fig. 1f** and **S10**), consistent with the TEM results and confirming that the oxide phases identified in microscopic analysis are also present in the bulk structure. Surface analysis by XPS (**Fig. S12**) exhibit a subtly different trend: both Cu-Cl and Cu-SO_4 NPs exhibited single peaks without distinct satellite features in the Cu 2p spectra, though the Cu-Cl peak was shifted toward a slightly higher binding energy. Because unambiguous oxidation state assignment from the Cu 2p peak positions alone is challenging, Cu LMM Auger electron spectroscopy was employed for a more definitive assessment (**Fig. 1g** and **S13**). In the LMM spectra, Cu-SO_4 NPs exhibited a signature characteristic of Cu^{2+}, whereas Cu-Cl NPs displayed a more pronounced feature characteristic of Cu^{+}. This result can be attributed to the substitutional incorporation of Cl within the particle lattice, which modifies the surface oxidation state of Cu. The absence of Cl-related reflections in the XRD patterns confirms that Cl is present in a doped, rather than a distinct crystalline phase, form. This interpretation was further corroborated by anion-specific XPS analysis: the Cl 2p spectrum of Cu-Cl NPs showed a single peak consistent with metal chloride bonding, no S signal was detected for Cu-SO_4 NPs, and only a minor sulfide signal was observed for Cu-Cl-SO_4 NPs (**Fig. 1h, S14,** and **S15**).

To further substantiate the differences in the surface chemical environment, O 1s XPS spectra were analyzed (**Fig. S16**). A striking contrast was observed between the two samples regarding the nature of their surface oxygen species. For the Cu-Cl NPs, the peak corresponding to lattice oxygen was notably minor; instead, the spectrum was characterized by a distinct component attributed to oxygen vacancies. This abundance of

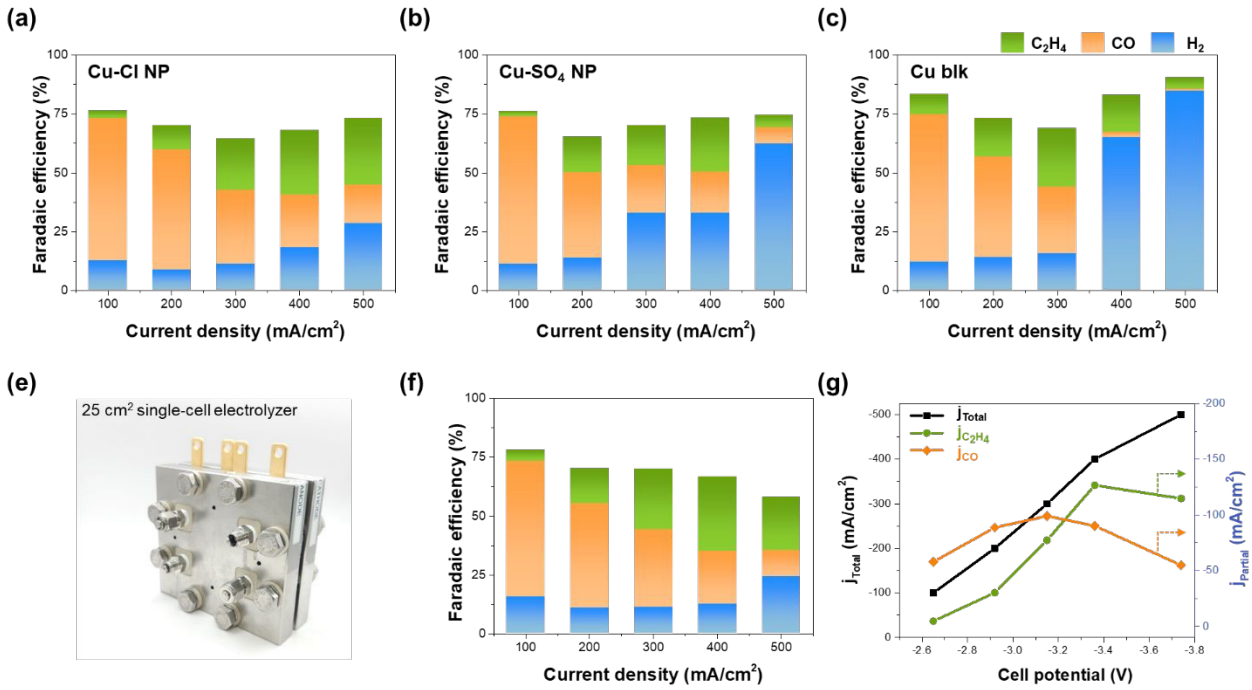

Fig. 2 CO_2RR performance of Cu-based catalysts under different cell configurations and electrolyte conditions. a–c) Faradic efficiencies for C_2H_4, CO, and H_2 measured in a 10 cm^2 MEA electrolyzer using 0.1 M $KHCO_3$ at current densities from 100 to 500 mA cm^{-2}, with a) Cu-Cl NPs, b) Cu-SO_4 NPs, and c) Cu blk. e–g) CO_2RR performance of Cu-Cl NPs in a 25 cm^2 single-cell electrolyzer using 0.5 M $KHCO_3$. e) Photograph of the 25 cm^2 single-cell electrolyzer, f) Faradic efficiencies, and g) total current densities and partial current densities for C_2H_4 and CO.

View Article Online
DOI: 10.1039/D6EY00070C

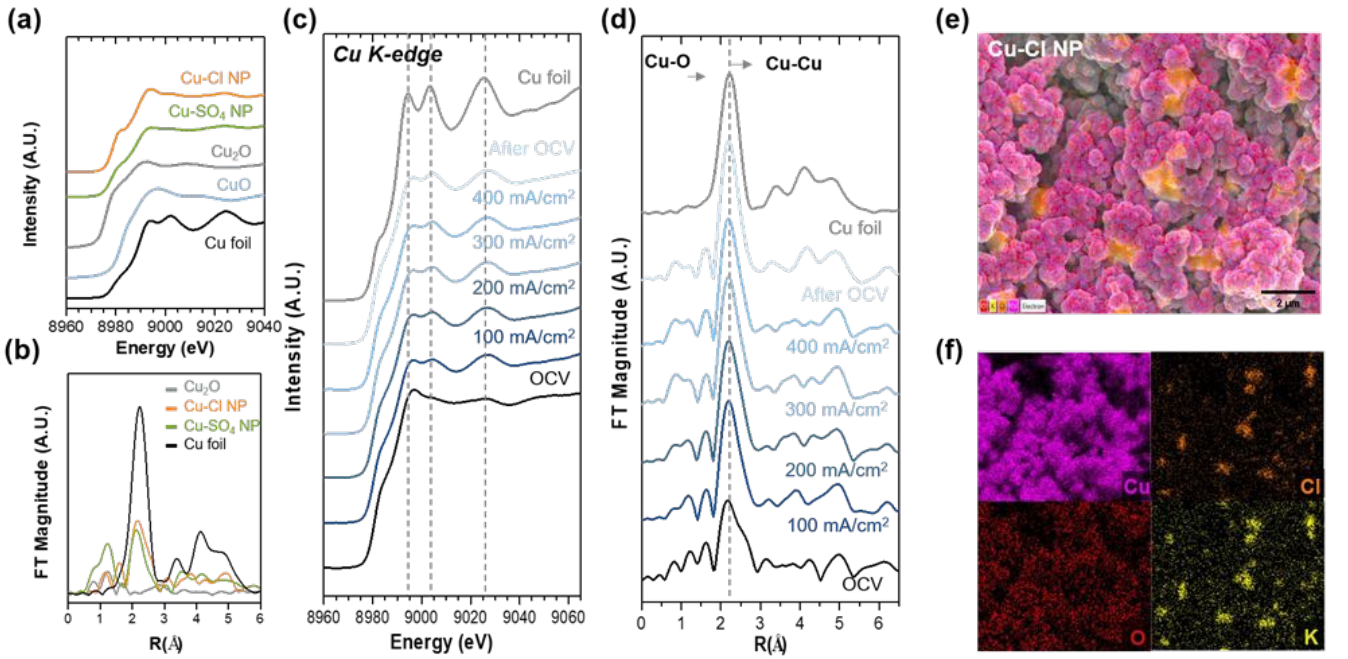

Fig. 3 a) XANES spectra of Cu-X NPs, b) EXAFS spectra of Cu-X NPs, c, d) operando XANES and FT-EXAFS spectra of Cu-Cl NPs measured at current densities from 100 to 400 mA cm^{-2} and after CO2RR, e) overlaid SEM-EDS mapping image of Cu-Cl NPs, f) individual SEM-EDS elemental maps of Cu, O, K, and Cl

oxygen vacancies supports the premise that the Cl incorporation induces the formation of defect-rich surface structures. In contrast, the O 1s spectrum of the Cu-SO_4 NPs was dominated by lattice oxygen, which is indicative of a well-developed metal oxide surface layer consistent with typical CuO phases. Furthermore, the complete absence of S 2p signals in Cu-SO_4 NPs—unlike the clear Cl signature in Cu-Cl NPs—confirms that the surface chemistry of Cu-SO_4 NPs is governed solely by intrinsic oxidation rather than anion modification, highlighting the unique role of Cl dopants in modulating the surface properties.

The electrochemical CO_2R performance of the synthesized catalysts was evaluated in a MEA electrolyzer with an active area of 10 cm^2, using 0.1 M $KHCO_3$ as the anolyte. Applied current density was increased stepwise from 100 to 500 mA cm^{-2} in increments of 100 mA cm^{-2}. The gas-phase products were analyzed by real-time gas chromatography (GC). As liquid products were not quantified in this study, the unaccounted FE is attributed to liquid products such as ethanol and non-Faradaic losses.

Distinct variations in the catalytic selectivity were observed as a function of precursor identities. For Cu-Cl NPs (**Fig. 2a**), CO was the dominant product at low current densities; however, as current density increased, the CO production declined, while C_2H_4 selectivity improved progressively. Specifically, the C_2H_4 FE reached 27.7% at 400 mA cm^{-2} and peaked at 28.2% at 500 mA cm^{-2}. In this range, the catalyst effectively suppresses the competing hydrogen evolution reaction (HER). By contrast, the Cu-SO_4 NPs prepared under otherwise identical conditions (**Fig. 2b**) exhibited comparable performances at low-current densities; however, HER increased sharply beginning at 300 mA cm^{-2}, indicating an inability to suppress the competing reaction at higher currents. A similar trend was observed for commercial Cu NPs (Cu blk) used as a reference (**Fig. 2c**), where hydrogen evolution increased steeply from 400 mA cm^{-2}. For Cu-Cl-SO_4 NPs, the FE for C_2 products at low current densities was comparable to that of Cu-Cl NPs owing to the influence of Cl anions; however, device failure occurred at high current densities indicating insufficient structural stability under harsh electrochemical conditions (**Fig. S17**). Taken together, the Cu-Cl NPs demonstrated superior performance by effectively suppressing the HER and maintaining high C_2H_4 selectivity, at high current densities in the MEA system. This enhancement was attributed to the substitution of Cl species on the catalyst surface, as confirmed by the characterization data above, which modulates the oxidation state of Cu, thereby strengthening the CO adsorption and promoting the C–C coupling to facilitate C_2H_4 formation.

To further assess the scalability and practical applicability of the catalyst, performance was evaluated in a larger-scale MEA device with an active area of 25 cm^2 (**Fig. 2d**). Consistent catalytic behavior was observed in the scaled-up system, mirroring the trends identified in the 10 cm^2 device: CO production was dominant at lower current densities, whereas C_2H_4 FE peaked under high-current conditions (**Fig. 2e**). Notably, the catalyst achieved a maximum C_2H_4 FE of 31% at 400 mA cm^{-2} in the larger system. The voltage–current density profile (**Fig. 2f**) confirmed stable operation of the large-area cell. Beyond the electrochemical performance, this work also addresses a practical challenge in scaling-up maintaining catalyst uniformity during synthesis. Our ambient-condition, liquid-phase synthesis approach offers a distinct advantage in this regard, proving well-suited for the mass production required for large-area device implementation.

Additionally, to evaluate the long-term stability of this performance, we conducted long-term durability tests using devices with different geometric electrode areas. At a current density of 200 mA cm^{-2}, the device with a 10 cm^2 electrode area operated stably for 95 hours (**Fig. S18**). Although an increase in cell voltage was observed over time, the Faradaic efficiency was successfully maintained without significant degradation. When the same experiment was replicated using a 25 cm^2 device, a rapid performance decline occurred within a few hours (**Fig. S19**). A post-reaction analysis revealed that while the catalyst itself showed no noticeable changes from its pristine state, salt precipitation had formed within the flow channels, obstructing the CO_2 gas supply. These findings indicate that while the catalyst possesses excellent inherent performance and long-term durability, discrepancies arise from the device-specific optimization required for long-term evaluations. This underscores that enhancing performance in CO_2RR requires not only advancing catalyst efficiency but also addressing engineering challenges for practical upscaling.

To investigate the mechanistic origins of the distinct performance differences, XAFS analysis at the Cu K-edge was performed on the prepared electrodes. The *ex situ* X-ray absorption near-edge structure (XANES) spectra revealeded distinct electronic features depending on the precursor used (**Fig. 3a**). The Cu-SO_4 electrode exhibited a smooth oscillation profile after the main absorption peak, closely resembling the characteristic features of copper oxide species. By contrast, the Cu-Cl electrode displayed well-defined second and third oscillation peaks that were closely aligned with those of the metallic Cu foil, indicating a substantial metallic character in the bulk structure. A critical distinguishing feature, however, is a markedly more pronounced shoulder peak relative to the Cu foil reference. This shoulder is attributed to the Cu_2O, suggesting that a distinct surface oxidation state exists in the Cu-Cl electrode, unlike in the nominally metallic phase.

The local atomic arrangement was investigated by Fourier transform (FT) analysis of the extended XAFS (EXAFS) spectra (**Fig. 3b**), with the Cu foil spectrum serving as a reference for the standard Cu–Cu bond position. The FT spectrum of the Cu-Cl electrode exhibited a main peak at approximately 2.2 Å, consistent with the Cu–Cu bond distance of the Cu foil, indicating a predominantly metallic coordination environment. Conversely, the Cu-SO_4 electrode showed a dominant peak at a shorter radial distance of approximately 1.6 Å, corresponding to Cu–O bonds. This distinction confirmed that the Cu-Cl catalyst possessed a metallic framework, whereas the Cu-SO_4 catalyst was primarily composed of copper oxide species.

The structural transformation of the Cu-Cl catalyst under CO_2 reduction conditions was then investigated via *operando* XANES analysis (**Fig. 3c**). Measurements were conducted by increasing the current density stepwise from 100 to 400 mA cm^{-2}, followed by a return to open-circuit voltage (OCV) to track the phase evolution of the electrode. At the initial OCV stage, the spectrum exhibiteds a mixed state characterized by the coexistence of metallic Cu and oxide features, rather than a fully oxidized phase. Upon applying a reduction current, the catalyst underwent a rapid phase transition, to a metallic state, closely resembling that of metallic copper. Notably, this metallic phase was maintained throughout operation up to 400 mA cm^{-2}. This structural stability is consistent with the GC analysis, in which a high C_2H_4 FE was sustained up to 400 mA cm^{-2} without degradation. Furthermore, upon terminating the reaction and returning to the OCV in the electrolyte, the catalyst did not revert to its initial oxidized state but retained the metallic Cu phase. This irreversible change indicates that the catalyst surface underwent electrochemical reconstruction during the reaction, forming a robust and stable active phase.

A detailed analysis of the *operando* EXAFS FT spectra provides further evidence of this structural behavior (**Fig. 3d**). At OCV, the Cu–Cu coordination shell appears as a split-peak structure: the primary peak at shorter radial distance corresponds to metallic Cu–Cu bonds, whereas the subsequent shoulder feature is characteristic of Cu–Cu scattering within an oxide lattice, confirming the presence of crystalline oxide phases within the electrode at OCV. Upon applying a reduction potential, the electrode underwent rapid reduction and the spectrum was dominated by a strong metallic Cu-Cu peak. However, a distinctive behavior is observed with respect to the oxygen-related features. The shoulder peak corresponding to Cu–Cu bonds in the oxide lattice disappears—indicating collapse of the long-range crystalline oxide structure—the Cu–O peak at approximately 1.6 Å does not completely vanish but persists at low intensity. This implies that, although the bulk oxide is reduced, local oxygen species, likely in the form of chemisorbed or subsurface oxygen, remain on the surface. These residual oxygen species are believed to play a critical role in maintaining the catalytically active Cu^+ sites under reductive conditions, preventing complete reduction of the catalyst to an inert metallic phase. Notably, the Cu–O to Cu–Cu peak ratio remains largely unchanged with increasing current density, demonstrating the robust maintenance of these catalytic properties.

In contrast to the Cu-Cl NPs, Cu-SO_4 NPs exhibited a markedly different structural evolution under identical *operando* conditions (**Fig. S20**). Although a gradual reduction was observed, the EXAFS spectra of Cu-SO_4 NPs displayed a persistent and dominant peak at approximately 1.3 Å even at current densities up to 400 mA cm^{-2}. This peak corresponds to the Cu–O coordination shell, indicating that the Cu-SO_4 NPs failed to fully transition to the metallic phase and retained substantial bulk oxide character throughout the reaction. The intensity of this peak decreased with increasing current density, consistent with the observed decline in the catalytic performance. This reduction behavior suggests that the oxygen species in the Cu-SO_4 NPs exist as stable, bulk-like oxides, rather than the beneficial subsurface oxygen observed in the Cu-Cl NPs. Consequently, this uncontrolled oxide phase likely fails to provide the precise electronic modulation required for C–C coupling and instead favoring the competing hydrogen evolution, as reflected in the electrochemical performance data. This interpretation is further supported by post-reaction analysis. The SEM images collected after the CO_2RR experiment reveal a rough morphology and a slight increase in the particle size relative to the pristine state (**Fig. S21**), indicating

View Article Online
DOI: 10.1039/D6EY00070C

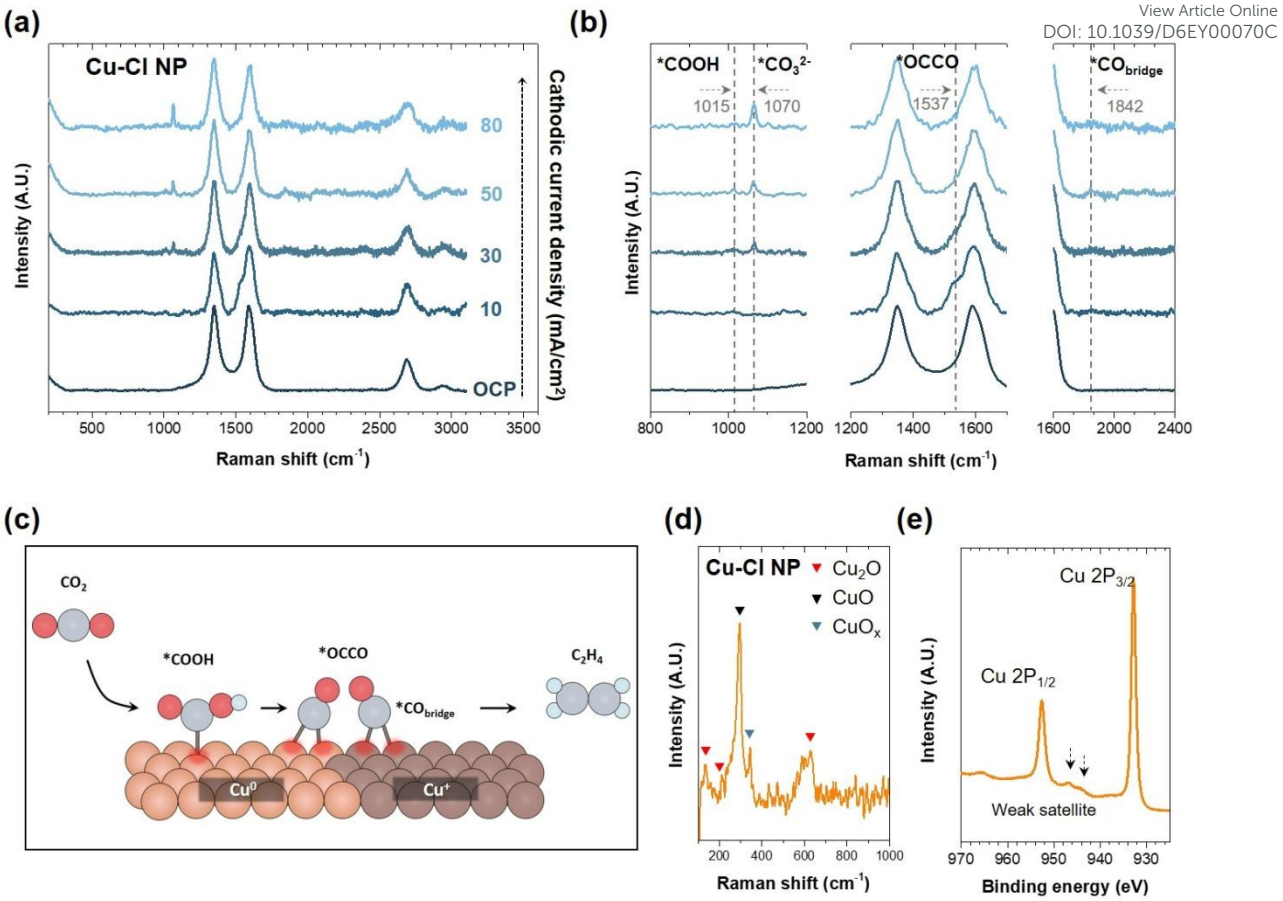

Fig. 4 a, b) *In situ* Raman spectra of Cu-Cl NPs under CO_2RR conditions in CO_2-saturated 0.1 M $KHCO_3$. The spectra were acquired using a 532 nm laser excitation source. Chronoamperometry was performed with a current density range from open-circuit potential to 80 mA/cm². c) Schematic illustration of the proposed CO2RR mechanism at the Cu^{2+}/Cu^{+} interfaces. d) *Ex-situ* Raman spectrum of Cu-Cl NPs. e) XPS Cu 2p spectrum of Cu-Cl NPs.

reconstruction-induced coarsening during the reaction. Interestingly, distinct cubic crystals were sporadically observed on the electrode surface alongside the copper particles. Elemental mapping (**Fig. 3e** and **3f**) identified these structures as KCl. This observation provides a critical clue regarding the fate of the dopants: it suggests that the doped chloride, originally incorporated within the lattice, underwent surface segregation as the copper surface experienced electrochemical reconstruction under reductive potentials. The segregation of these chloride ions locally increased the negative charge density at the electrode–electrolyte interface, promoting the enrichment of K^+ from the electrolyte. Upon drying after the reaction, these enriched species precipitated as crystalline KCl. By contrast, EDS analysis of the Cu-SO_4 electrode after the reaction (**Fig. S22**) revealed no precipitation or residual sulfur signals, effectively ruling out external contamination. This post-reaction evidence strongly corroborates the conclusion that chloride was intrinsic to the catalyst structure and participated in dynamic surface evolution through this anion-driven cation enrichment process.

To analyze the reduction mechanism associated with the formation of reaction intermediates, *in situ* Raman spectroscopy was performed on the Cu-Cl NP electrode under CO_2RR conditions (**Fig. 4a, b**). Measurements were conducted by increasing the current density stepwise from OCV. Noting that vigorous bubble evolution at higher rates scatters the incident light and distorts the optical path, measurement range was limited up to 80 mA cm^{-2} to ensure reliable spectra collection. The evolution of the Raman peaks enabled tracking of the surface environment and identification of key reaction intermediates[50-52].

Regarding changes in the surface environment during CO_2RR, the emergence of a peak at 1015 cm^{-1} is assigned to the *COOH intermediate, providing direct spectroscopic evidence of CO_2 adsorption and activation on the electrode surface. The peak at 1070 cm^{-1} is attributed to $*CO_3^{2-}$, indicative of local pH increase and subsequent carbonate formation as the reaction proceeds. The intensity of this peak increases with current density, reflecting the accelerated CO_2RR kinetics at higher applied currents.

The two prominent peaks in the 1200–1600 cm^{-1} range are the D and G bands originating from the carbon paper substrate, which also serves as the gas diffusion layer. A shoulder peak appearing at 1537 cm^{-1} on the low-wavenumber side of the G band with increasing current is assigned to the *OCCO stretching mode, signifying C–C coupling between the CO intermediates and serving as direct spectroscopic evidence of C_2H_4 production on the Cu-Cl NP electrode. Additionally, a weak peak at 1842 cm^{-1} is assigned to bridge-bonded CO, which is also considered to contribute to *OCCO intermediate formation.

View Article Online DOI: 10.1039/D6EY00070C

This experimental observation of facilitated C-C coupling is consistent with recent density functional theory (DFT) and ab initio molecular dynamics (AIMD) reports[37, 53-56]. These theoretical studies demonstrate that specifically adsorbed halide ions modulate the interfacial charge distribution, lowering energy barrier for CO-CO dimerization to promote C_{2+} selectivity.

These sequential intermediate features, illustrated in the mechanistic scheme in **Fig. 4c**, confirm the reaction pathway from CO_2 adsorption and activation through C–C coupling to C_2H_4 formation. Furthermore, *ex situ* Raman spectra—consistent with the XRD data—revealed a complex surface composition comprising CuO, Cu_2O, and Cl-doped CuO_x species. This mixed-valence surface state is further supported by the weak satellite peaks observed in the Cu 2p XPS spectra (**Fig. 4d, e**), in agreement with the proposed reaction mechanism.

The *in situ* Raman spectra of the Cu-SO_4 NP electrode (**Fig. S23**) reveal a different trend. At low current densities, the higher relative intensity of the $*CO_3^{2-}$ peak (1085 cm^{-1}) compared to the $*COO^-$ peak (1033 cm^{-1}) indicates that CO_2 is not being effectively activated toward the reduction pathway. Furthermore, the presence of the *OCHO peak at 1275 cm^{-1}, combined with the absence of a distinct *OCCO peak, suggests that the reaction on the Cu-SO_4 surface is kinetically hindered from proceeding to the C–C coupling stage.

Conclusions

In summary, we have established that the choice of precursor anion is not merely a synthetic variable but also a critical factor in determining the active phase dynamics of Cu electrocatalysts. Using a $CuCl_2$ precursor, we incorporated an intrinsic chloride species that directed the formation of a defect-rich cubic-like nanostructure. These precursor-derived chloride dopants play pivotal roles in modulating the surface electronic environment, thereby stabilizing the thermodynamically unstable Cu^+ active sites. This structural configuration results in superior catalytic performance and scalability. The Cu-Cl catalyst achieved a C_2H_4 FE of 31% at 400 mA cm^{-2} in a large-area (25 cm^2) MEA electrolyzer. The synthesis method also demonstrated high feasibility for mass production, yielding gram-scale quantities in a single batch under ambient conditions. *Operando* XAFS analysis provided direct mechanistic insight, revealing a stark contrast in structural evolution: the sulfate-derived catalyst failed to fully reduce and retain a bulk oxide phase that favors hydrogen evolution, and the chloride-derived catalyst transformed into a robust metallic phase with persistent local oxygen species. This active phase, sustained by the dopant-induced surface environment, is critical for selective C2H4 formation. Collectively, these findings highlight the overlooked potential of precursor engineering as a facile yet powerful strategy for modulating electrocatalyst performance. Based on these insights, future research should strategically optimize co-doping with other halide species to maximize the efficacy. Introducing secondary anions (e.g., bromide or iodide) with stronger covalent affinity offers a promising strategy to overcome the high-rate performance limitations. This co-doping approach effectively suppresses the dynamic copper reconstruction that otherwise diminishes active halide coverage under aggressive polarization, enabling further ethylene enrichment.

Experimental

Synthesis of Cu-X NP

Copper(II) chloride dihydrate ($CuCl_2{\cdot}2H_2O$, Sigma-Aldrich, 221783), copper(II) sulfate ($CuSO_4$, Sigma-Aldrich, 61230), and sodium borohydride ($NaBH_4$, Sigma-Aldrich, 213462) were employed as starting materials. Cu NPs were synthesized via a scalable wet-chemical reduction method at ambient temperature and pressure. A 0.2 M copper precursor solution (100 mL) was prepared by dissolving the respective copper salt in deionized (DI) water. Separately, a $NaBH_4$ solution (100 mL) was prepared as the reducing agent. Under vigorous stirring, $NaBH_4$ solution was added dropwise to the copper precursor solution. The reaction was allowed to proceed until hydrogen gas evolution ceased, ensuring complete reduction. This liquid-phase approach is highly amenable to mass production, yielding approximately gram-scale quantities of NPs per laboratory-scale batch. The resulting precipitates were collected by centrifugation and washed thoroughly with DI water and ethanol at least three times to remove soluble byproducts and loosely adsorbed ions. The washed samples were then freeze-dried for 24 h to prevent particle aggregation. The final products synthesized from the chloride and sulfate precursors are denoted as Cu-Cl NPs and Cu-SO_4 NPs, respectively.

Characterization

XRD (Bruker D8 Advance) was performed using Cu K_α radiation (λ = 0.154 nm) to characterize the crystalline structure. The morphological and compositional features of the Cu NPs were examined by field-emission SEM (FE-SEM, Hitachi Regulus8250) combined with EDS. The oxidation states of the Cu NPs were analyzed by XPS (Ulvac Co., PHI 5000 Versaprobe). The morphology of the Cu-Cl and Cu-SO_4 NPs was further characterized by HR-TEM (Titan G2 Cube 60-300, FEI).

Preparation of Electrodes

Preparation of working electrodes (cathodes)

Working electrodes were fabricated by spray-coating a catalyst ink onto a carbon paper substrate (39BB, Sigracet). The ink was prepared by dispersing the synthesized Cu NPs in isopropyl alcohol with a Nafion binder solution and sonicating for 20 min to ensure a homogeneous dispersion. The catalyst loading was controlled at 1.0 mg cm^{-2}. For large-area electrode fabrication, an automated spray system was used to ensure uniform catalyst layer distribution across the expanded active area. The coated electrodes were dried at ambient temperature prior to cell assembly.

Preparation of counter electrodes (anodes)

IrO_2 anodes were fabricated on Pt–Ti felt (5GDL05N-035, 0.35 mm, Bekaert, Zevegem) by thermal decomposition. An IrO_2 precursor solution was prepared by dissolving 100 mg of

View Article Online
DOI: 10.1039/D6EY00070C

$IrCl_3 \cdot xH_2O$ (203491, Sigma-Aldrich) in a 1:3 (v/v) mixture of 36% HCl (4090-4400, Daejung) and isopropyl alcohol (IPA) with continuous stirring for 24 h. The Pt–Ti felt was fully submerged in the prepared solution and subsequently annealed in a box furnace at 500 °C for 1 h.

Electrochemical Device Testing

The CO_2 reduction performance of the Cu NP- electrodes was assessed in a custom-built MEA electrolyzer comprising a serpentine titanium flow plate, an IrO_2/Pt–Ti foam anode for the oxygen evolution reaction (OER), customized alignment gaskets, and a commercial anion-exchange membrane (PiperION® AEM, Versogen). A 0.1 M $KHCO_3$ aqueous solution was used as the anolyte and circulated by a peristaltic pump. High-purity humidified CO_2 was introduced into the gas flow channel at 200 sccm and reduced to the target products at the catalyst surface. The gas-phase products were analyzed online by GC (Agilent 7890A) equipped with a water trap at the inlet to prevent moisture interference from the argon carrier gas. Carbon-containing gases (CO, CH_4, and C_2H_4) and H_2 were detected using flame ionization detector (FID) and thermal conductivity detectors (TCD), respectively. The FE of each gaseous product was calculated as follows:

$$FE_{product}(\%) = \frac{i_{product}}{i_{total}} \times 100 = \frac{V_{product} \times Q \times \frac{2F_P}{RT}}{i_{total}} \times 100,$$

where F, Q, T, and R denote the Faraday constant (96,485 C mol^{-1}), product flow rate, temperature (298 K), and ideal gas constant (8.314 J mol^{-1} K^{-1}), respectively. As liquid products were not quantified in this study, the unaccounted FE is attributed to the liquid products and system losses.

Operando X-ray Absorption Spectroscopy

Cu K-edge hard X-ray absorption spectroscopy (XAS) spectra of the Cu-Cl NPs, Cu-SO_4 NPs, Cu blk, Cu foil, Cu_2O, and CuO were recorded at the 1D beamline of the Pohang Accelerator Laboratory. *In situ* and *operando* XAS measurements were conducted using a custom electrochemical MEA cell equipped with a 10 cm^2 electrode and a 1 cm^2 aperture for X-ray transmission. The counter electrodes were IrO_2/Pt-Ti foam and a 0.1 M $KHCO_3$ electrolyte was circulated through the anodic compartments. Detailed setup information is provided in a previous report.[10]

In Situ Raman Spectroscopy

Raman spectroscopy was performed on the Cu-X NP electrodes using an inVia Raman Microscope (Renishaw) equipped with a 532 nm laser. For *in situ* measurements, a three-electrode cell configuration was employed. Spectra were acquired at various current densities normalized to the active surface area.

Author contributions

Jiho Jeon, Sohui Kim: Conceptualization, Data curation, Writing – original draft. Min Gwan Ha, Dogyeong Kim, Hyeon-Seok Bang, Young-Jin Ko: Investigation, Resources. Jae-Young Choi: Resources, Data curation. Dongmok Whang, Woong-Hee Lee, Hyung-Suk Oh: Funding acquisition, Supervision, Project administration

Conflicts of interest

There are no conflicts to declare.

Data availabilit

A Supplementary information is available.
Data can be made available upon reasonable request.

Acknowledgements

J.J. and S.K. contributed equally to this work. This work was supported by institutional program grants from the Korea Institute of Science and Technology (KIST) and the National Research Foundation of Korea (NRF) funded by the Ministry of Science and ICT (MSIT) (Grant No. RS-2023-00302697), Republic of Korea. This research was also supported by the National Research Council of Science & Technology (NST) grant funded by the Korea government (MSIT) (No. GTL25021-210). We are grateful for access to the 1D PAL beamline for Operando XAFS.

Notes and references

1. A. R. Woldu, Z. Huang, P. Zhao, L. Hu and D. Astruc, Coord. Chem. Rev., 2022, 454, 214340.
2. J. F. D. Tapia, J.-Y. Lee, R. E. H. Ooi, D. C. Y. Foo and R. R. Tan, Sustain. Prod. Consum., 2018, 13, 1–15.
3. W. H. Lee, K. Kim, J. H. Koh, D. K. Lee, H.-S. Oh, U. Lee and B. K. Min, Nano Energy, 2023, 110, 108373.
4. G. Wang, J. Chen, Y. Ding, P. Cai, L. Yi, Y. Li, C. Tu, Y. Hou, Z. Wen and L. Dai, Chem. Soc. Rev., 2021, 50, 4993–5061.
5. S. Nitopi, E. Bertheussen, S. B. Scott, X. Liu, A. K. Engstfeld, S. Horch, B. Seger, I. E. Stephens, K. Chan and C. Hahn, Chem. Rev., 2019, 119, 7610–7672.
6. T. Lu, T. Xu, S. Zhu, J. Li, J. Wang, H. Jin, X. Wang, J. J. Lv, Z. J. Wang and S. Wang, Adv. Mater., 2023, 35, 2310433.
7. H. Leflay, J. Pandhal and S. Brown, Journal of CO2 Utilization, 2021, 52, 101657.
8. S. Chen, J. Liu, Q. Zhang, F. Teng and B. C. McLellan, Renew. Sustain. Energy Rev., 2022, 167, 112537.
9. H.-S. Bang, J. Jeon, J. Kang, Y.-J. Ko, C. Oh, H. Kim, X. Zhang, K. H. Choi, C. Woo, X. Dong, H. K. Yu, W. H. Lee, J.-Y. Choi and H.-S. Oh, Small, 2024, 20, 2404343.
10. J. Jeon, H.-S. Bang, Y.-J. Ko, E. Huh, J. Kang, X. Zhang, S. Ka, Y. Kim, W. H. Lee, K. Kim, H. K. Yu, H.-S. Oh and J.-Y. Choi, Chem. Eng. J., 2025, 523, 168350.
11. J. Jeon, H. S. Bang, Y. J. Ko, J. Kang, X. Zhang, C. Oh, H. Kim, K. H. Choi, C. Woo and X. Dong, Small Methods, 2024, 2401157.
12. C. A. Obasanjo, A. S. Zeraati, H. S. Shiran, T. N. Nguyen, S. M. Sadaf, M. G. Kibria and C.-T. Dinh, J. Mater. Chem. A, 2022, 10, 20059–20070.
13. H. P. Duong, N.-H. Tran, G. Rousse, S. Zanna, M. W. Schreiber and M. Fontecave, ACS Catal., 2022, 12, 10285–10293.
14. Y. Chen, R. K. Miao, C. Yu, D. Sinton, K. Xie and E. H. Sargent, Matter, 2024, 7, 25–37.

15. R. Chauhan, R. Sartape, N. Minocha, I. Goyal and M. R. Singh, Energy & Fuels, 2023, 37, 12589–12622.
16. H.-S. Bang, Y.-J. Ko, H. S. Jeon, E. Huh, E. D. Kim, M. G. Ha, C. Lim, J. Jeon, S. Ka, D. Kim, X. Zhang, Y. Kim, K. Kim, W. H. Lee, J.-Y. Choi and H.-S. Oh, Adv. Funct. Mater., 36, e11894.
17. I. Amghizar, L. A. Vandewalle, K. M. Van Geem and G. B. Marin, Engineering, 2017, 3, 171–178.
18. P. De Luna, C. Hahn, D. Higgins, S. A. Jaffer, T. F. Jaramillo and E. H. Sargent, Science, 2019, 364, eaav3506.
19. M. Jouny, W. Luc and F. Jiao, Industrial & Engineering Chemistry Research, 2018, 57, 2165–2177.
20. H. Shin, K. U. Hansen and F. Jiao, Nat. Sustain., 2021, 4, 911–919.
21. S. C. da Cunha and J. Resasco, ACS Energy Lett., 2024, 9, 5550–5561.
22. A. R. Woldu, Z. Huang, P. Zhao, L. Hu and D. Astruc, Coord. Chem. Rev., 2022, 454.
23. X. He, L. Lin, X. Li, M. Zhu, Q. Zhang, S. Xie, B. Mei, F. Sun, Z. Jiang, J. Cheng and Y. Wang, Nat. Commun., 2024, 15, 9923.
24. B. S. Crandall, Z. Qi, A. C. Foucher, S. E. Weitzner, S. A. Akhade, X. Liu, A. R. Kashi, A. K. Buckley, S. Ma, E. A. Stach, J. B. Varley, F. Jiao and J. Biener, Small, 2024, 20, 2401656.
25. Y. Hori, A. Murata and R. Takahashi, Journal of the Chemical Society, Faraday Transactions 1: Physical Chemistry in Condensed Phases, 1989, 85, 2309–2326.
26. F. Li, H. Tariq, H. Yang, Y. Cao, T. Zhou and G. Wang, ACS Catal., 2024, 14, 15088–15095.
27. W. Zhang, S. Zhao, X. Wang, L. Yang, Q. Zhao, C. Jiang, Y. Wang, Y. Wu and Y. Chen, ACS Nano, 2025, 19, 24023–24033.
28. L. Xiong, X. Fu, J. Zhang, S. Liu, S. Li, S. Lu, D. Wang and Q. Yue, Adv. Funct. Mater., 2025, 35, 2420161.
29. M. Zhang, Z. Chen and Y. A. Wu, Adv. Funct. Mater., 2026, 36, e29196.
30. S. Chen, C. Ye, Z. Wang, P. Li, W. Jiang, Z. Zhuang, J. Zhu, X. Zheng, S. Zaman, H. Ou, L. Lv, L. Tan, Y. Su, J. Ouyang and D. Wang, Angew. Chem., 2023, 135, e202315621.
31. J. Wang, Z. Liu, W. Jin, Y. Tuo, Y. Zhou, S. Zhou, T. Gong, J. Li, Y. Ni, M. Wang and L. Jiang, Applied Catalysis B: Environment and Energy, 2025, 375, 125434.
32. R. He, K. Huang, X. Yang, J. Xu and Z. Tong, Chem. Eng. J., 2024, 502, 158067.
33. J. Wang, H. Yang, Q. Liu, Q. Liu, X. Li, X. Lv, T. Cheng and H. B. Wu, ACS Energy Lett., 2021, 6, 437–444.
34. H. Wang, Q. Wu, R. Du and G. Chen, ACS Appl. Mater. Interfaces, 2025, 17, 55003–55012.
35. M. Jun, J. Kundu, D. H. Kim, M. Kim, D. Kim, K. Lee and S.-I. Choi, Adv. Mater., 2024, 36, 2313028.
36. Y. Zhou, Y. Yao, R. Zhao, X. Wang, Z. Fu, D. Wang, H. Wang, L. Zhao, W. Ni, Z. Yang and Y.-M. Yan, Angew. Chem. Int. Ed., 2022, 61, e202205832.
37. J. J. Masana, B. Peng, Z. Shuai, M. Qiu and Y. Yu, J. Mater. Chem. A, 2022, 10, 1086–1104.
38. S.-C. Lin, C.-C. Chang, S.-Y. Chiu, H.-T. Pai, T.-Y. Liao, C.-S. Hsu, W.-H. Chiang, M.-K. Tsai and H. M. Chen, Nat. Commun., 2020, 11, 3525.
39. D. Gianolio, M. D. Higham, M. G. Quesne, M. Aramini, R. Xu, A. I. Large, G. Held, J.-J. Velasco-Vélez, M. Haevecker, A. Knop-Gericke, C. Genovese, C. Ampelli, M. E. Schuster, S. Perathoner, G. Centi, C. R. A. Catlow and R. Arrigo, ACS Catal., 2023, 13, 5876–5895.
40. J.-J. Velasco-Velez, R. V. Mom, L.-E. Sandoval-Diaz, L. J. Falling, C.-H. Chuang, D. Gao, T. E. Jones, Q. Zhu, R. Arrigo, B. Roldan Cuenya, A. Knop-Gericke, T. Lunkenbein and R. Schlögl, ACS Energy Lett., 2020, 5, 2106–2111.
41. C. Yang, B. H. Ko, S. Hwang, Z. Liu, Y. Yao, W. Luc, M. Cui, A. S. Malkani, T. Li, X. Wang, J. Dai, B. Xu, G. Wang, D. Su, F. Jiao and L. Hu, Sci. Adv., 2020, 6, eaaz6844.
42. C. D. Koolen, E. Oveisi, J. Zhang, M. Li, O. V. Safonova, J. K. Pedersen, J. Rossmeisl, W. Luo and A. Züttel, Nat. Synth., 2023, 3, 47–57.
43. M. G. Kim, J. Park, Y. Choi, H. C. Song, S. H. Kim, K. M. Bang, H. C. Ham, N. K. Kim, D. H. Won and B. K. Min, Advanced Energy Materials, 2023, 2300749.
44. Y. Wang, L. Cheng, W. Ge, Y. Zhu, J. Zhang, R. Chen, L. Zhang, Y. Li and C. Li, ACS Appl. Mater. Interfaces, 2023, 15, 23306–23315.
45. M. Li, S. Kuang, H. Liu, Q. Fan, S. Zhang and X. Ma, J. Phys. Chem. C, 2023, 127, 3952–3959.
46. Y. Zhang, X.-Y. Zhang and W.-Y. Sun, ACS Catal., 2023, 13, 1545–1553.
47. Y. Yang, S. Louisia, S. Yu, J. Jin, I. Roh, C. Chen, M. V. Fonseca Guzman, J. Feijóo, P.-C. Chen, H. Wang, C. J. Pollock, X. Huang, Y.-T. Shao, C. Wang, D. A. Muller, H. D. Abruña and P. Yang, Nature, 2023, 614, 262–269.
48. S. H. Lee, J. E. Avilés Acosta, D. Lee, D. M. Larson, H. Li, J. Chen, J. Lee, E. Erdem, D. U. Lee, S. J. Blair, A. Gallo, H. Zheng, A. C. Nielander, C. J. Tassone, T. F. Jaramillo and W. S. Drisdell, Journal of the American Chemical Society, 2025, 147, 6536–6548.
49. Q.-m. Liu, D.-b. Zhou, Y. Yamamoto, R. Ichino and M. Okido, Transactions of Nonferrous Metals Society of China, 2012, 22, 117–123.
50. H. Li, P. Wei, D. Gao and G. Wang, Current Opinion in Green and Sustainable Chemistry, 2022, 34, 100589.
51. Z.-Y. Du, K. Wang, S.-B. Li, Y.-M. Xie, J.-H. Tian, Q.-N. Zheng, W. F. Ip, H. Zhang, J.-F. Li and Z.-Q. Tian, J. Phys. Chem. C, 2024, 128, 11741–11755.
52. J. Zhang, H. Gao, Z. Wang, H. Gao, L. Che, K. Xiao and A. Dong, Nanomaterials, 2025, 15, 1517.
53. S. A. Akhade, I. T. McCrum and M. J. Janik, J. Electrochem. Soc., 2016, 163, F477.
54. H. Li, T. Liu, P. Wei, L. Lin, D. Gao, G. Wang and X. Bao, Angew. Chem. Int. Ed., 2021, 60, 14329–14333.
55. X. Mao, T. He, G. Kour, H. Yin, C. Ling, G. Gao, Y. Jin, Q. Liu, A. P. O'Mullane and A. Du, Chemical Science, 2024, 15, 3330–3338.
56. Y. Jiang, H. He, D. Xia, H. Zhang, S. Tan, L. Luo, Y. Kong, L. Deng and Y.-N. Liu, Green Chemistry, 2025, 27, 9737–9745.

View Article Online
DOI: 10.1039/D6EY00070C

Data Availability Statement

A Supplementary information is available. Data can be made available upon reasonable request.